LANGMUIR

pubs.acs.org/Langmuir Article

Lipid Membrane Interaction of Peptide/DNA Complexes Designed for Gene Delivery

Neval Yilmaz, Yutaka Kodama, and Keiji Numata*

Cite This: *Langmuir* 2021, 37, 1882−1893 Read Online

ACCESS | Metrics & More | Article Recommendations | Supporting Information

ABSTRACT: Among gene delivery systems, peptide-based gene carriers have received significant attention because of their selectivity, biocompatibility, and biodegradability. Since cellular membranes function as a barrier toward exogenous molecules, cell-penetrating peptides (CPPs), which are usually cationic and/or amphiphilic, can serve as efficient carriers to deliver cargo into the cytosol. Here, we examined the interactions of carrier peptides and their DNA complexes with lipid membranes using a quartz crystal microbalance (QCM) and high-speed atomic force microscopy (HS-AFM). The carrier peptides are a 12-residue partial presequence of yeast cytochrome *c* oxidase subunit IV (Cytcox) and BP100, which are a mitochondria-targeting signal peptide and a CPP, respectively. QCM data showed that BP100 has a higher binding affinity than Cytcox to both plasma membrane- and mitochondrial membrane-mimicking lipid bilayers. The DNA complexes with either Cytcox or BP100 exhibited the same tendency. Furthermore, HS-AFM data demonstrated that the DNA complexes of either peptide can disrupt the lipid membranes, forming larger pores in the case of Cytcox. Our results suggest that the binding affinity of the peptide/DNA complex to the plasma membrane is more critical than its membrane disruption ability in enhancing the cellular uptake of DNA.

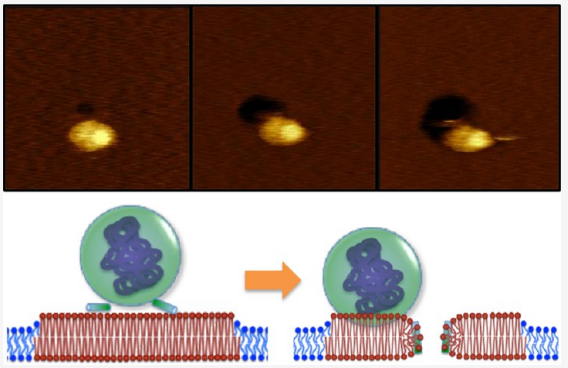

INTRODUCTION

Gene delivery systems, which are important for gene therapy, gene modification, and gene editing, face numerous barriers in both extracellular and intracellular environments. Among nonviral gene delivery systems, there is growing interest in peptide-based carriers because of their effectiveness in compacting genetic material, biocompatibility, and biodegradability.[1−3] For successful gene delivery from the extracellular environment to the intracellular target, the carrier peptides should be able to penetrate the cell membrane, escape from the endosome, and transport the genetic material to the correct organelle. Cell-penetrating peptides (CPPs), which are usually short cationic and/or amphiphilic peptides, have been widely explored as carrier peptides to transport cargo into the intracellular environment.[4−8] The internalization of CPPs and their cargo-carrying complexes into the cell takes place via direct membrane penetration or endocytic pathways.[4,9] Delivery into subcellular compartments such as nuclei and mitochondria can be achieved by modification of CPPs with organelle-targeting sequences.[10]

In the efficient translocation of the carrier peptide and its DNA-carrying complex into the cell and organelle interior, membrane−peptide and membrane−complex interactions play a vital role.[11,12] Studies on peptide and peptide/DNA complex translocation are mostly performed using confocal fluorescence microscopy to assess their uptake and investigate their distribution inside living cells. Although this technique is indispensable, because of its limited resolution, the initial stages of translocation through the cell and organelle membranes remain unresolved. To understand how the peptide and the peptide/DNA complex interact with these membranes and penetrate them, higher-resolution techniques that can be applied in aqueous media are necessary. Atomic force microscopy (AFM), which is a powerful tool for the characterization of biological surfaces and structures at nanometer to subnanometer resolution under physiological conditions,[13] may shed light on the initial stages of the translocation process. This technique has been widely used for examining the action of antimicrobial peptides on model lipid membranes.[14] Several AFM studies involve CPPs as well;[15−18] however, there are no studies showing the dynamic behaviors of the peptide/DNA complex on lipid membranes.

Here, we aim to understand how the peptide and the peptide/DNA complex interact with and penetrate the cell membrane and the mitochondrial outer membrane. Among the targeted organelles for gene therapy, mitochondria have received

Received: November 18, 2020
Revised: January 1, 2021
Published: January 13, 2021

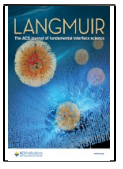

https://dx.doi.org/10.1021/acs.langmuir.0c03320
Langmuir 2021, 37, 1882−1893

considerable attention because of the various diseases originating from mitochondrial dysfunction.[19] For peptide-based mitochondria-targeted delivery, mitochondria-targeting peptides (MTPs) originating from endogenous proteins that bind to the mitochondrial membrane are advantageous due to their biocompatibility.[20] MTPs can be combined with CPPs to overcome two major barriers, the cell membrane and the mitochondrial membrane.[10] In the present study, we used an MTP consisting of the first 12 residues of the presequence of yeast cytochrome *c* oxidase subunit IV (Cytcox). The complexation of this peptide with plasmid DNA followed by its modification with a copolymer of lysine and histidine (KH_9),[21] which condenses the plasmid DNA and improves the transfection efficiency, results in successful delivery of DNA into the mitochondrial matrix.[22] To understand how the cellular uptake of an MTP/DNA complex is improved by CPPs, we compared the Cytcox and Cytcox-KH_9/DNA complexes with BP100 and the BP100-KH_9/DNA complex. BP100 is an antimicrobial peptide exhibiting CPP properties as well.[22−26] Its significant role in the delivery of the Cytcox-KH_9/DNA complex into the intracellular environment was reported for plant cells.[23]

To analyze the dynamic behaviors of the peptides and the peptide/DNA complexes mentioned above, we employed DPPC/DOPC/Chol (1:1:1) and DOPC/DOPE/PI/DOPS (5:3:1:1) lipid membranes as mimetic models of the mammalian plasma membrane (denoted plasma-MM) and the mitochondrial outer membrane (denoted mito-MM), respectively. We determined the lipid compositions of plasma-MM and mito-MM based on the reported lipid compositions and the suggested models of the eukaryotic plasma membrane[27−29] and the mitochondrial outer membrane.[30−32] We examined the membrane binding affinity of the peptides and the peptide/DNA complexes by the quartz crystal microbalance (QCM) technique and the influence of the peptide conformation by circular dichroism (CD) spectroscopy. We followed their action on the membranes using high-speed atomic force microscopy (HS-AFM),[33] which can provide in situ images of dynamic biological systems at a much higher time resolution than conventional AFMs. Thus, the results presented herein help identify both the characteristics of a peptide-based gene delivery system and the initial stages of the translocation process. Based on these results, the mechanism for the internalization of the peptide/DNA complex, i.e., direct membrane penetration or endocytic pathways, is also discussed.

MATERIALS AND METHODS

Materials. 1,2-Dipalmitoyl-*sn*-glycero-3-phosphocholine (DPPC) (850355C), 1,2-dioleoyl-*sn*-glycero-3-phosphocholine (DOPC) (850375C), 1,2-dioleoyl-*sn*-glycero-3-phosphoethanolamine (DOPE) (850725C), 1,2-dioleoyl-*sn*-glycero-3-phospho-L-serine (sodium salt) (DOPS) (840035C), and L-α-phosphatidylinositol (sodium salt) (liver PI) (840042C) were purchased from Avanti Polar Lipids, Inc. (Alabaster, AL). Cholesterol (Chol) (C 8667) was supplied from Sigma-Aldrich, Inc. (St. Louis, MO). Multilamellar vesicles (MLVs) of DPPC/DOPC/Chol (1:1:1) and DOPC/DOPE/PI/DOPS (5:3:1:1), mimicking the phase-separated plasma-MM and the mito-MM, were prepared at a total lipid concentration of 1 mM in solutions of phosphate-buffered saline (D-PBS; pH = 7.4) and 10 mM HEPES with 150 mM NaCl (pH = 7.4), respectively. D-PBS (045-29795), HEPES (340-01371), and NaCl (195-15975) were supplied by FUJIFILM Wako Pure Chemical Corp. (Osaka, Japan). MLVs were extruded through a polycarbonate membrane with a 100 nm pore size (NanoSizer MINI, T & T Scientific Corp.; Knoxville, TN). The specifications for the peptides and the plasmid DNA used in this study are provided by Chuah et al.[22,23] in detail. The peptide sequences were MLSLRQSIRFFK for Cytcox and KKLFKKILKYL for BP100. They were synthesized by the Research Resources Center of RIKEN (Wako, Japan). The plasmid DNA was phMGFP plasmid from Promega (Madison, WI). The Cytcox-KH_9/DNA and BP100-KH_9/DNA complexes were prepared at an N/P ratio of 0.5, where N is the number of amine groups in the peptide and P is the number of phosphate groups in the DNA.

Quartz Crystal Microbalance (QCM) Measurements. QCM measurements were performed at 24 °C with AFFINIX Q4 (Initium Inc., Tokyo, Japan). Twenty-seven MHz gold-coated quartz crystal sensor cells were used after cleaning with 1% (w/v) sodium dodecyl sulfate solution and piranha solution (3:1 mixture of sulfuric acid with 30% hydrogen peroxide). Supported lipid bilayers (SLBs) were prepared by the incubation of 10 μL of the lipid vesicles on the gold-coated sensors, followed by rinsing with the same buffer solution used for the preparation of lipid vesicles and Milli-Q water to remove the unfused vesicles. The sensor cells were filled with 450 μL of buffer solution. Ten microliters of peptide solution was injected into the sensor cells at certain time intervals. Binding of peptide to the SLBs caused a decrease in the frequency of the oscillating crystal. According to the Sauerbrey equation, the shift in the frequency is linearly proportional to the adsorbed mass. The shift in the frequency was plotted as a function of peptide concentration to determine the binding or association constant (K_a) on the basis of the Langmuir isotherm.[34] At least three repeats were used for determining each K_a value. The experimental data were fit to the Langmuir isotherm equation using Igor Pro from Wavemetrics, Inc. (Lake Oswego, OR).

Circular Dichroism (CD) Spectroscopy. CD spectra were measured at 24 °C with a Jasco J-820 CD spectropolarimeter (Jasco Inc., Tokyo, Japan). A 0.1 cm path length quartz cuvette was used after cleaning with piranha solution (3:1 mixture of sulfuric acid with 30% hydrogen peroxide). Unilamellar lipid vesicles were prepared in Milli-Q water at a total lipid concentration of 1 mM. The suspensions of unilamellar lipid vesicles with a size of approximately 100 nm were mixed with peptides at a peptide:lipid molar ratio of 1:50 or 1:40. The resultant peptide concentration was 20 or 25 μM. Background scans were obtained for 1 mM lipid vesicles. The background spectra were subtracted from the spectra collected in the presence of peptides. Each spectrum was the average of five scans. The spectra were collected from 190 to 240 nm at a rate of 100 nm/min and a resolution of 1 nm.

Size and ζ-Potential Measurements. Size and ζ-potential measurements for the peptide/DNA complexes were performed using a Zetasizer Nano-ZS (Malvern Instruments, Ltd.; Worcestershire, U.K.) as described in previous studies.[25,35]

High-Speed Atomic Force Microscopy (HS-AFM) Imaging. HS-AFM imaging was performed at room temperature by a Nanoexplorer (RIBM, Tsukuba, Japan). SLBs were prepared by the incubation of 1.5 μL of unilamellar lipid vesicles on a 1.5 mm diameter mica disk, followed by extensive rinsing as described above for the QCM measurements. The SLB-deposited mica surface was imaged in 70−80 μL of buffer solution with cantilevers containing silicon nitride (BL-AC10DS-A2) or carbon nanofiber (BL-AC10FS-A2) probes (Olympus Co.; Tokyo, Japan). Both cantilevers had a spring constant of 0.1 N/m and a resonance frequency between 450 and 500 kHz in aqueous media. The scan direction for image acquisition was from left to right, and the scan rate was 0.5 or 0.1 frame/s. After observation of the planar lipid bilayer, peptide or peptide/DNA complexes were introduced into the imaging medium. Plane leveling and line correction, when necessary, were applied to the HS-AFM images using Gwyddion.[36]

RESULTS AND DISCUSSION

Peptide and Complex Binding to the Plasma-MM and Mito-MM. First, we measured the time-dependent change in the response of the lipid membrane-modified QCM sensors in the presence of peptides to compare the peptide−membrane binding affinities. The time-course plots showed a discrete shift in the sensor frequency after the addition of peptides, indicating their binding to the membrane (Figures S1, S2). The binding or

https://dx.doi.org/10.1021/acs.langmuir.0c03320
Langmuir 2021, 37, 1882−1893

association constants (K_a) were calculated for each peptide on the basis of the Langmuir isotherm and are listed in Table 1. For

Table 1. Association Constants (K_a) of the Peptides for the Lipid Membranes

lipid membrane	peptide	$K_a \times 10^{-6}$ (M^{-1}) average ± s.d.
plasma-MM	Cytcox	0.63 ± 0.10
	BP100	1.97 ± 0.36
	Cytcox-KH_9	3.97 ± 0.71
	BP100-KH_9	14.65 ± 3.35
mito-MM	Cytcox	1.84 ± 0.49
	BP100	3.13 ± 0.90
	Cytcox-KH_9	5.21 ± 1.17
	BP100-KH_9	5.49 ± 0.25

both the plasma-MM and mito-MM, the K_a values of BP100 were higher than those of Cytcox, indicating the stronger interaction of BP100 with the membranes. The K_a value of BP100 was almost fourfold that of Cytcox on plasma-MM, whereas it was less than twofold the Cytcox value for mito-MM. Both peptides exhibited higher binding affinity to mito-MM than to plasma-MM.

To assess the possible origin of the variation in the membrane binding affinities of Cytcox and BP100, we measured their CD spectra in the absence and presence of the liposomes. Cytcox and BP100 were unstructured in both the absence and presence of the liposomes of the plasma-MM (Figure 1a). This result implies that the higher binding affinity of BP100 than that of Cytcox was not caused by differences in their secondary structure in the plasma-MM. However, we cannot rule out the possibility of an undetectably low degree of structure in the plasma-MM and contributions of the unbound peptides to the profile of the CD spectra. In the presence of liposomes of the mito-MM, the CD spectra for Cytcox and BP100 showed minima at approximately 207 and 222 nm (Figure 1b) due to the α-helical structure attained by these peptides in the mito-MM. Indeed, the subunit IV precursors of yeast cytochrome *c* oxidase[37−39] and BP100[40,41] were reported to form considerable amounts of α-helix in only the presence of negatively charged lipids.

We also compared the membrane binding affinities of Cytcox-KH_9 and BP100-KH_9, which were used to form peptide/DNA complexes in this study. The KH_9 domain improved the peptide−membrane interaction, especially for the plasma-MM. The K_a values of Cytcox-KH_9 and BP100-KH_9 were calculated to be six- to sevenfold higher on the plasma-MM and two- to threefold higher on the mito-MM than those for Cytcox and BP100. Interestingly, the K_a values of Cytcox-KH_9 and BP100-KH_9 were similar on the mito-MM due to a threefold decrease in the K_a value of BP100-KH_9 on the mito-MM relative to the plasma-MM. A comparison between the complexes of these peptides with plasmid DNA revealed that the amounts of the BP100-KH_9/DNA complex bound to both the plasma-MM and mito-MM were higher than those of the Cytcox-KH_9/DNA complex (Figure 2). The difference between the membrane-

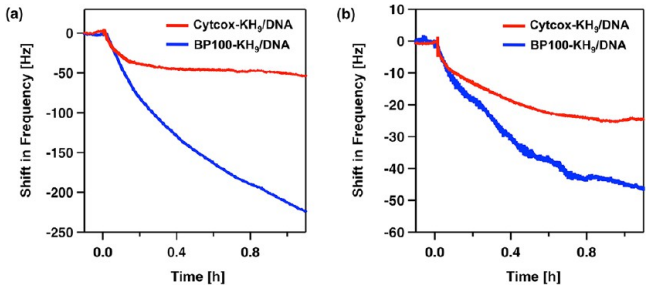

Figure 2. Time-course plots showing the binding of the Cytcox-KH_9/DNA and BP100-KH_9/DNA complexes to the plasma-MM (a) and mito-MM (b). The volumes of solutions with the complexes added to the QCM sensor cells in (a) and (b) were 10 and 20 μL, respectively.

bound amounts of these complexes was larger for the plasma-MM (Figure 2a) than for the mito-MM (Figure 2b). This is in agreement with the differences in the K_a values of Cytcox and BP100 shown in Table 1, where the variation for the plasma-MM is larger than that for the mito-MM.

Peptide-Induced Morphological Changes in the Plasma-MM. We visualized the changes in the morphology of the plasma-MM in the presence of peptides using HS-AFM. Figures 3−5 show that the plasma-MM consists of the DPPC-rich taller phase and the DOPC-rich shorter phase. The DPPC-rich phase is liquid ordered (L_o) because of the presence of Chol, and the DOPC-rich phase is liquid disordered (L_d).[42,43] After the addition of Cytcox into the imaging medium, the shorter domains appeared in the L_o phase (indicated by arrows in Figure 3a). We attributed the appearance of these domains to membrane thinning.[16,44−47] These domains were approximately

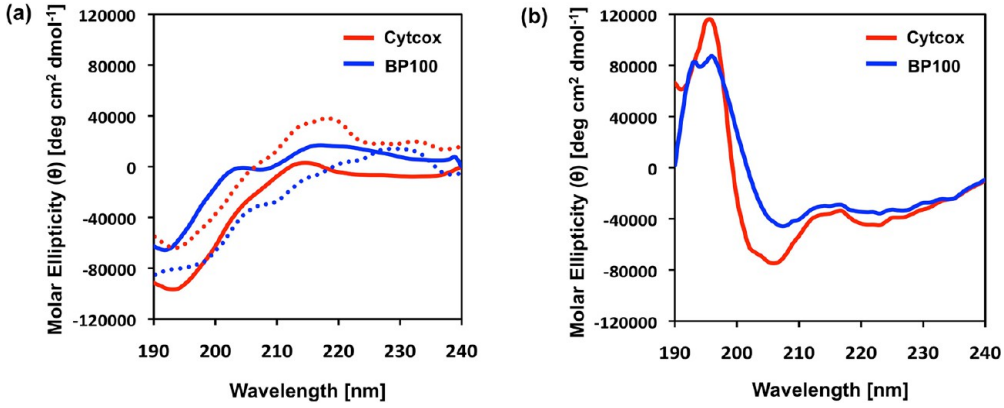

Figure 1. CD spectra of Cytcox and BP100 in the presence of the lipid vesicles of plasma-MM (a) and mito-MM (b). The total lipid concentration was 1 mM. The peptide:lipid molar ratios in (a) and (b) were 1:50 and 1:40, respectively. The CD spectra of Cytcox and BP100 measured in the absence of lipid vesicles are shown as dotted lines in (a) (red-dotted, Cytcox; blue-dotted, BP100).

https://dx.doi.org/10.1021/acs.langmuir.0c03320
Langmuir 2021, 37, 1882−1893

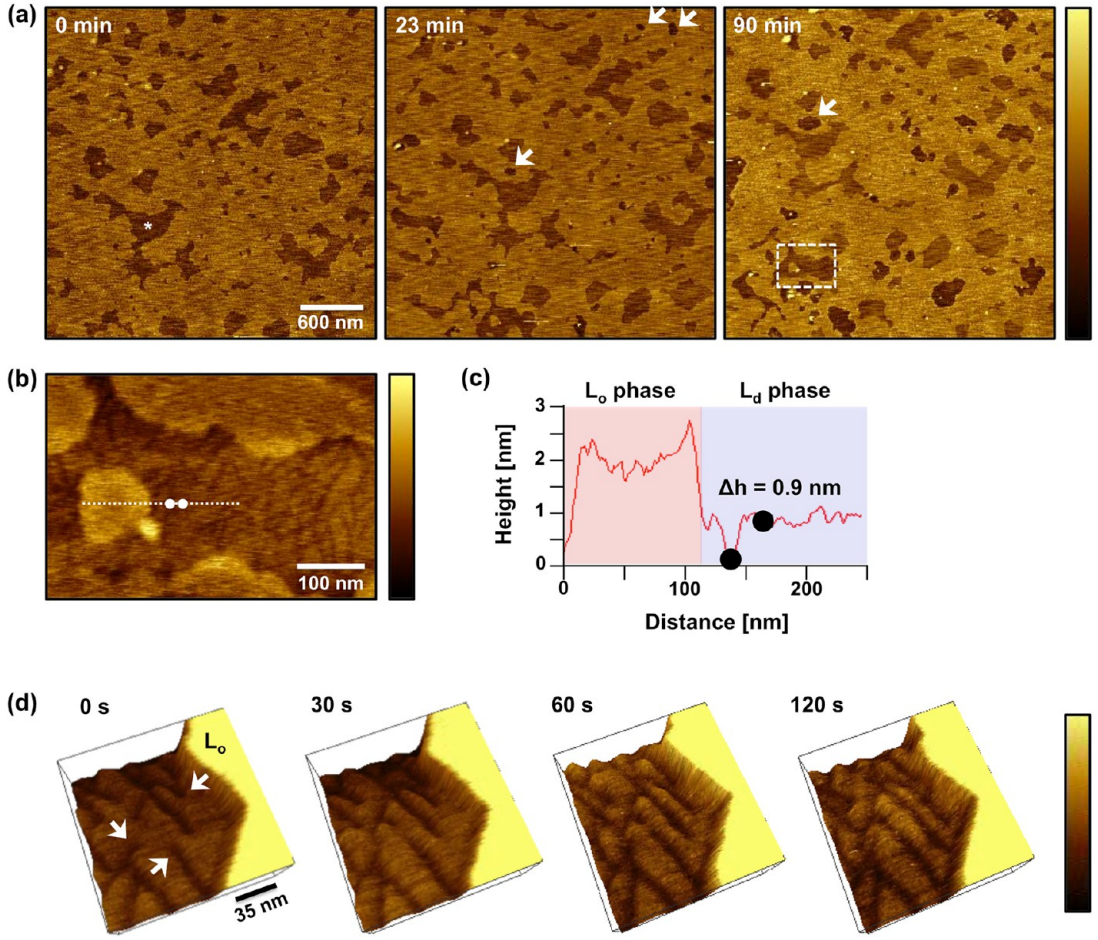

Figure 3. Cytcox-induced membrane thinning in the plasma-MM. (a) HS-AFM height images showing the changes in the plasma-MM in the presence of 25 μM Cytcox. The term "0 min" corresponds to the time just after the addition of Cytcox. The asterisk at 0 min denotes the L_d phase. The arrows indicate the short domains that formed during incubation with Cytcox. (b) Higher-resolution image of the region within the dashed line box in (a). (c) Height profile along the dashed line in (b). Δh represents the height difference between the black circles, which correspond to the white circles on the dashed line in (b). The red and blue zones denote the L_o and L_d phases, respectively. (d) HS-AFM height images showing the formation of long narrow defects in the L_d phase. The extending defects are indicated by the arrows. The color bar indicates the range of Z from 0 (darkest) to Z_{max} (brightest); Z_{max} = (a) 6, (b) 7, and (d) 4 nm.

1.5 nm thinner than the L_d domains. We also observed the formation of long narrow defects in these short domains and the L_d domains (Figure 3b). These defects were almost 1 nm shorter than the surrounding phase (Figure 3c) and extended continuously (Figure 3d). The HS-AFM images in Figure 3d were obtained in the same experimental set as those presented in Figure S3a. Figure S3a and Movie 1 show that the L_d phase enlarged with the formation of long narrow defects. In addition, porelike defects were visualized in some of the images (indicated by arrows in Figure S3b). The formation of porelike defects likely denotes lipid removal from the membrane.

In the presence of BP100, the L_d phase gradually spread to the membrane defects (Figure 4a), which were the lipid-free mica surface as proven both by the height profile and the phase image (Figure S4). The height of the lipid membrane from the mica surface was around 5 nm (Figures S4a, c), corresponding to the height of a single lipid bilayer, and the contrast in the phase image confirms that the underlying layer was the mica surface (Figure S4b), exhibiting different properties than the membrane. The gradual enlargement of the L_d phase caused the disappearance of these defects. The coverage of the exposed mica by the lipid membrane in the presence of BP100 is shown at a smaller scan area in Figure S3c and Movie 2. The enlargement of the L_d phase toward the L_o phase or the shrinkage of the L_o phase was not clearly observed in the presence of BP100, in contrast to the behavior of Cytcox. The height profiles along the dashed lines in Figure 4a show that the L_d phase was lowered by 0.5 nm during its expansion between 0 and 160 s (Figure 4b). The observed membrane thinning might have resulted from the parallel alignment of BP100 at the membrane interface and a subsequent reduction in the lipid acyl chain order, which would lead to an increase in the occupied lipid area and hence the sealing of the membrane defects. Indeed, BP100 aligns parallel to the membrane interface by localizing between the lipid acyl chains and the headgroups as an α-helix;[40,48] however, we did not detect a helical structure by CD measurement (Figure 1a). We assume that it has a similar alignment even when unstructured or with a low degree of helicity. In short, both Cytcox and BP100 induced membrane thinning while being unstructured in the plasma-MM. However, the changes induced by Cytcox in the plasma-MM were more complex than those induced by BP100.

The alterations induced in the plasma-MM by Cytcox-KH_9 and BP100-KH_9 were strikingly different from those observed in the presence of Cytcox and BP100. In contrast to Cytcox and BP100, both Cytcox-KH_9 and BP100-KH_9 disrupted the

https://dx.doi.org/10.1021/acs.langmuir.0c03320
Langmuir 2021, 37, 1882−1893

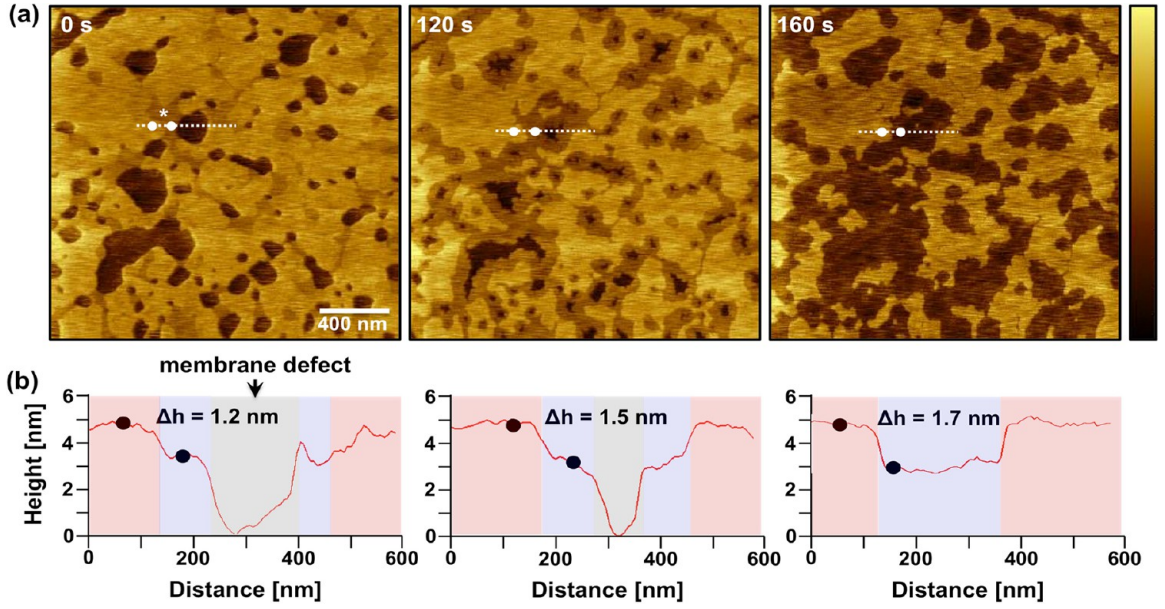

Figure 4. BP100-induced membrane thinning in the plasma-MM. (a) HS-AFM height images showing the changes in the plasma-MM in the presence of 9 μM BP100. The term "0 s" corresponds to 1.5 min after the addition of BP100. The asterisk at 0 s denotes the L_d phase. The color bar indicates the range of Z from 0 (darkest) to Z_{max} (brightest); Z_{max} = 11 nm (0 s), 9 nm (120 s), and 6 nm (160 s). (b) Height profiles along the dashed lines in (a). Δh represents the height difference between the black circles, which corresponds to the white circles on the dashed lines in (a). The red, blue, and gray zones denote the L_o and L_d phases and the membrane defect, respectively.

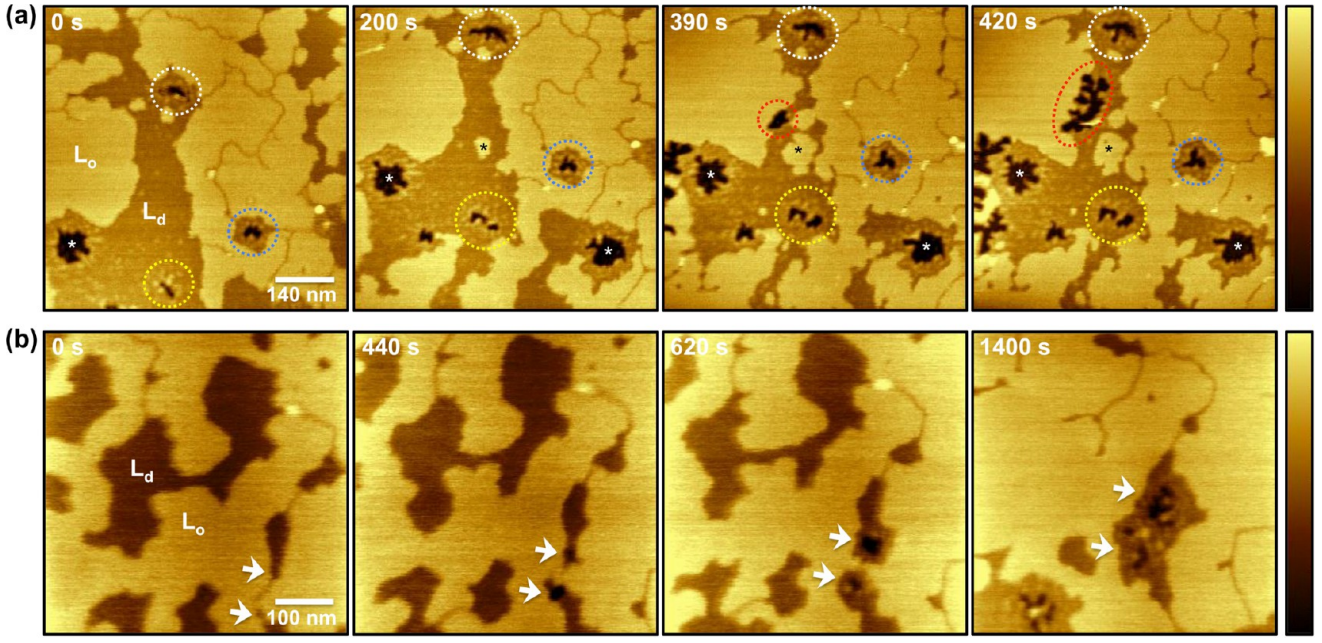

Figure 5. Cytcox-KH_9- and BP100-KH_9-induced membrane disruption in the plasma-MM. (a) HS-AFM height images showing the changes in the plasma-MM in the presence of 3 μM Cytcox-KH_9. The term "0 s" corresponds to 18 min after the addition of Cytcox-KH_9. The asterisks mark the stable pores. The white, yellow, and blue circles indicate the pores that enlarged slowly. The red circle indicates a pore that formed and enlarged very fast. (b) HS-AFM height images showing the changes in the plasma-MM in the presence of 0.5 μM BP100-KH_9. The term 0 s corresponds to 2 min after the addition of BP100-KH_9. The arrows point to the growing pores. The color bar indicates the range of Z from 0 (darkest) to Z_{max} (brightest); Z_{max} (a, b) = 5 nm.

membrane via the formation of pores (Figure 5, Movies 3–5), which usually exhibited branching due to diffusion-limited disruption.[49] Since disruption at this level was not observed in the presence of Cytcox or BP100, pore formation must have been induced by the insertion of the polycationic KH_9 domains into the membrane. KH_9 might have created toroidal pores by causing the lipid headgroups to bend inward as suggested for highly cationic arginine-rich peptides.[50,51] In the presence of Cytcox-KH_9, as visualized in Movie 3, some of the pores did not enlarge (e.g., pores marked with asterisks in Figure 5a) or only grew slightly (e.g., pores within the white, yellow, and blue circles in Figure 5a). In contrast, the pore in the red circle, which appeared at the L_o/L_d phase boundary, rapidly grew, indicating that the phase boundary, where the hydrophobic mismatch

https://dx.doi.org/10.1021/acs.langmuir.0c03320
Langmuir 2021, 37, 1882−1893

between the lipid acyl chains in the L_o and L_d phases exists, facilitates the crowding of these peptides and their pore formation. A close view of the pore formation at the phase boundary is shown in Figure S5a. Pore formation occurred at a much lower concentration for BP100-KH_9 than Cytcox-KH_9, and all of the pores seemed to grow continuously or trigger further disruption (Figure 5b, Figure S5b, and Movies 2, 3). This is highly likely due to the higher binding affinity of BP100-KH_9 than Cytcox-KH_9, allowing the recruitment of a higher number of BP100-KH_9 molecules to the membrane. As the pores grew, the L_d domains in which no visible pores were detected shrank, and simultaneously, the area of the L_o phase increased. The coalescence of the L_o domains and the shrinkage of the pore-free L_d phase imply tighter packing of lipids in the pore-free regions. Before the appearance of pores, the L_d phase slightly enlarged instead of shrank, possibly because of the parallel alignment of the peptide to the membrane interface at low surface concentrations. In addition, pores were surrounded by domains shorter than the L_o phase, and these domains enlarged with the growing pores. This might imply that the peptide molecules aligned parallel to the membrane interface around the pores trigger disruption via pore formation above a threshold concentration. At the later stages of disruption, considerable amounts of aggregates accumulated around the pores, indicating the ejection of lipids from the membrane.

Peptide-Induced Morphological Changes in the Mito-MM. There were no significant changes in the morphology of the mito-MM at low peptide concentrations. In the presence of Cytcox and BP100, it was especially difficult to distinguish the peptide-induced changes in the membrane (Figures S6a, S7a). Neither pore formation nor sealing of the membrane defects was observed. The patchy structure formed by BP100 on the mito-MM might have resulted from the formation of a thin layer on the membrane or local thinning in the membrane (Figure S7a). In the presence of Cytcox-KH_9 and BP100-KH_9, changes in the mito-MM cells were clearer. At elevated peptide concentrations, we observed the formation of a thin amorphous layer on the membrane (Figures S6b and S7b, c), suggesting the surface adsorption of the peptides. The existence of the thin layer in the form of domains (Figure S7c) may indicate the clustering of anionic lipids from zwitterionic lipids.[47,52] The surface adsorption of the peptides on the anionic membrane was possibly facilitated via electrostatic interactions, especially in the presence of the highly cationic Cytcox-KH_9 and BP100-KH_9. Therefore, these peptides might be locked on the membrane surface[53] or partly penetrate into the membrane.[54] They did not rupture the mito-MM by forming visible pores, in contrast to the zwitterionic plasma-MM. The membrane edges were the only regions that underwent some changes during incubation with the peptides, and membrane disruption took place by the formation of lipid/peptide aggregates (Movies 6 and 7). The existence of the thin layer on the membrane and the formation of the lipid/peptide aggregates suggest the disruption of the membrane via the carpet mechanism and detergent-like action of the peptides.[55] Nevertheless, we should not rule out the possibility of the translocation of these peptides across the membrane by the formation of undetectably small transient pores.[53,54]

Complex-Induced Morphological Changes in the Plasma-MM and Mito-MM. After we examined the peptide-induced morphological changes in the lipid membranes using HS-AFM, we studied the morphology and dynamics of the DNA complexes. When fused with the KH_9 domain, Cytcox and BP100 can form compact and efficient complexes with plasmid DNA.[22,23] As characterized by the DLS measurement, the Cytcox-KH_9/DNA and BP100-KH_9/DNA complexes prepared in this work had a size of around 162 and 137 nm, respectively (Figure S8a). The size of the BP100-KH_9/DNA complex was slightly smaller than the that of Cytcox-KH_9/DNA complex, indicating the formation of a more compact complex by BP100. These complexes exhibited negative zeta potential due to the excess amount of plasmid DNA in the complex prepared at N/P 0.5 (Figure S8b). The HS-AFM images showed that the Cytcox-KH_9/DNA and BP100-KH_9/DNA complexes usually appeared as intact particles on the plasma-MM; i.e., peptide and plasmid DNA remained associated with the membrane. We did not observe the plasmid DNA alone on the membrane surface, which might indicate the efficient complexation of plasmid DNA with the peptides despite the excess amount of plasmid DNA. Some of the complex particles showed a clear morphology with a dense, coiled structure when imaged at a high force, indicating the condensation of plasmid DNA by the peptides (Figures 6a–c). These complexes also seemed to have inserted into the membrane (Figures 6a–c, Figure S9). Under mildly acidic conditions, as visualized for the Cytcox-KH_9/DNA complex (Figure S10), the complex exhibited a slightly unfolded coil (Figure S10a) or exposed its DNA-rich region (Figure S10b).

Both Cytcox-KH_9/DNA and BP100-KH_9/DNA complexes were localized on the DPPC-rich L_o domains of the plasma-MM (Figures 6d, g, Figures S11a, b). Their binding to the L_o domains caused membrane thinning and/or disruption. Because of membrane thinning or fluidization, the complex was localized at the L_o/L_d phase boundary or in the L_d phase, as shown in Figure 6 and Figure S11. In the presence of the Cytcox-KH_9/DNA complex, either fluidization or disruption was observed (Figures 6d, e). The Cytcox-KH_9/DNA complex disrupted the L_o domains of the membrane by creating pores that were round with uniform depth (Figure 6e, Figure S12). The pores formed in the vicinity of the complex and enlarged during observation. The pore depth indicated the formation of a nearly lipid-free defect in the membrane (Figure 6f) or the complete removal of the lipids in both the outer and inner leaflets of the membrane. The latter was more evident in the case of large pores (Figure S12b), during whose formation the complex started to dissociate. Around the BP100-KH_9/DNA complex, both fluidization and disruption occurred (Figure 6g). Figure 6h clearly shows the coexistence of the fluidized region, which was initially the L_o phase (Figure 6g), with the shorter disrupted regions. The height profile along the dashed line indicates that these shorter regions consisted of a complete pore and regions thinner than the surrounding fluidized membrane (Figure 6i). The height difference between the fluidized and thinner regions was 3 nm. This difference is slightly larger than the thickness of one lipid leaflet and therefore denotes the removal of only the outer leaflet of the membrane. These results, showing the coexistence of regions of different heights, suggest that the increased disorder in the membrane was followed by the subsequent removal of the outer- and inner-leaflet lipids and hence the gradual disruption of the membrane by the BP100-KH_9/DNA complex. The changes in the plasma-MM induced by both complexes are illustrated in Figure 7, where membrane fluidization and disruption are assumed to have been caused by the released peptide. I, II, and III indicate the membrane fluidization, disruption, and coexistence of both fluidized and disrupted regions, respectively.

https://dx.doi.org/10.1021/acs.langmuir.0c03320
Langmuir 2021, 37, 1882–1893

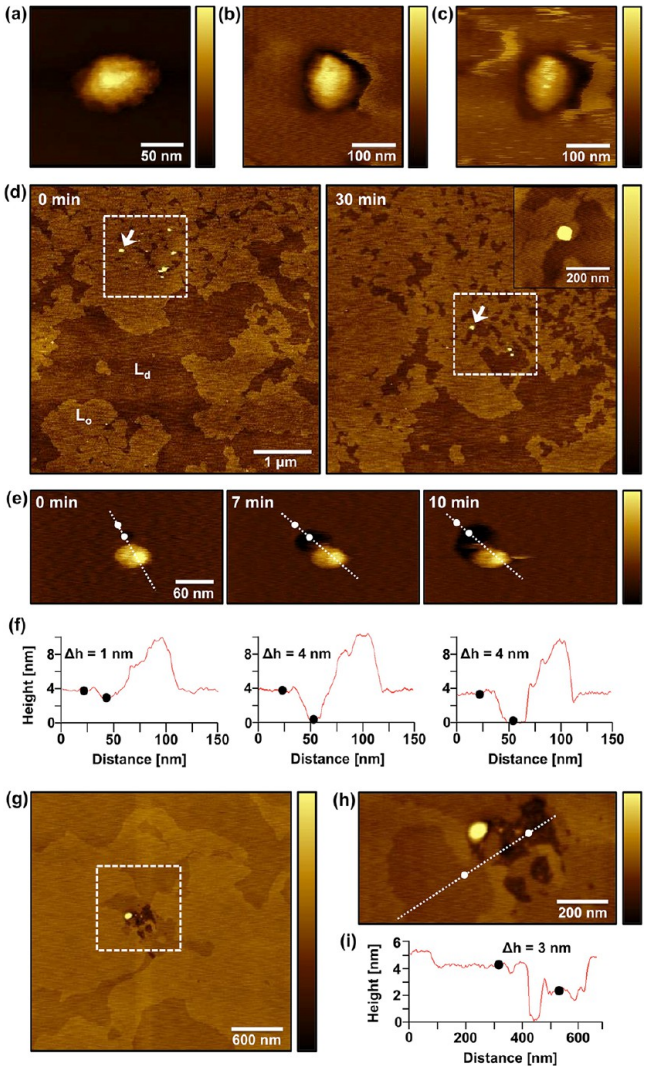

Figure 6. Peptide/DNA complexes localized on the plasma-MM and their membrane-disrupting activity. HS-AFM height images showing the Cytcox-KH_9/DNA complex (a) and the BP100-KH_9/DNA complex (b, c) on the plasma-MM. The image in (c) was captured at a higher imaging force. (d) HS-AFM height images showing the Cytcox-KH_9/DNA complex localized on the L_o domain of the plasma-MM during membrane fluidization. The dashed line box contains the region where fluidization was observed. Inset is an enlarged image of the complex indicated by the arrow within the dashed line box. (e) HS-AFM height images showing pore formation by the Cytcox-KH_9/DNA complex. The term "0 min" corresponds to 2.5 h in (d) and 1.5 h in (e) after the addition of 20 μL of complex into the imaging medium. The images in (d) and (e) were obtained in different experimental sets. (f) Height profiles along the dashed lines in (e). (g) HS-AFM height images showing the BP100-KH_9/DNA complex localized on the L_o domain of the plasma-MM after 4 h of incubation. (h) Higher-resolution image of the region within the dashed line box in (g). The time difference between the images in (g) and (h), which were recorded 1.5 h after the addition of the complex, was approximately 1 min. (i) Height profile along the dashed line in (h). The Δh in (f) and (i) represents the height difference between the black circles, which correspond to the white circles on the dashed lines in (e) and (h). The color bar indicates the range of Z from 0 (darkest) to Z_{max} (brightest): Z_{max} = (a) 22 nm, (b) 12 nm, (c) 18 nm, (d) 7 nm, (e) 7 nm (0 min), 11 nm (7, 10 min), and (g, h) 15 nm.

The Cytcox-KH_9/DNA and BP100-KH_9/DNA complexes also induced pore formation in the mito-MM (Figure 8a, c),

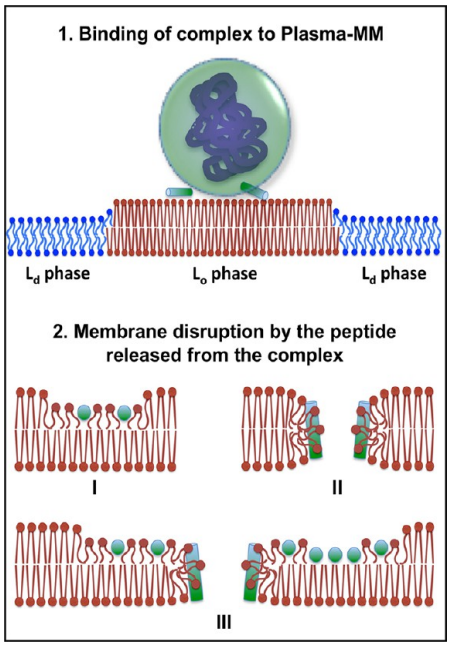

Figure 7. Illustration of membrane fluidization and disruption induced by Cytcox-KH_9 and BP100-KH_9 released from Cytcox-KH_9/DNA and BP100-KH_9/DNA complexes bound to the L_o domains of the plasma-MM. Plausible mechanism for the complex-induced changes in the membrane: fluidization or thinning due to the localization of the peptide within the polar/apolar interface of the membrane (I), toroidal pore formation due to the membrane deformation induced by the KH_9 domains, and gradual disruption in the membrane by a mixed effect of fluidization and removal of membrane leaflets (III).

although no pores were visualized in the mito-MM in the presence of Cytcox-KH_9 or BP100-KH_9. The pore depth was similar to the membrane thickness (Figure 8b, d), implying the removal of both outer and inner leaflets of the membrane. After prolonged incubation, the Cytcox-KH_9/DNA complex disrupted most of the membrane, and some of the complexes seemed to have dissociated, yielding DNA-like structures in the disrupted regions (Figure S13a). In contrast, we did not detect DNA-like features in the disrupted regions of the membrane in the presence of the BP100-KH_9/DNA complex. It either dissociated into small globular particles (Figure S13b) or stayed intact with the condensed DNA (Figure S13c).

Peptide–Membrane and Complex–Membrane Interactions. The QCM results showed that BP100, which is a CPP, has a higher membrane binding affinity than the mitochondria-targeting peptide Cytcox (Table 1). One reason for its higher binding affinity may be having more cationic residues than Cytcox. Similarly, the greater binding affinity of these cationic peptides for the negatively charged mito-MM than for the zwitterionic plasma-MM can also be attributed to the stronger peptide–membrane electrostatic attraction. For the mito-MM, we need to consider the effect of the peptide secondary structure as well, as Cytcox and BP100 were shown to attain an α-helical structure in the mito-MM (Figure 1b). However, the small difference between the K_a values of Cytcox and BP100 and the decrease in the K_a value of BP100-KH_9, which is the most cationic peptide studied herein, for the mito-MM relative to the plasma-MM indicate the contribution of another factor. Although electrostatic interactions are required for the initial binding of peptides to the membrane surface, their intensification may counteract hydrophobic interactions, which are

https://dx.doi.org/10.1021/acs.langmuir.0c03320
Langmuir 2021, 37, 1882−1893

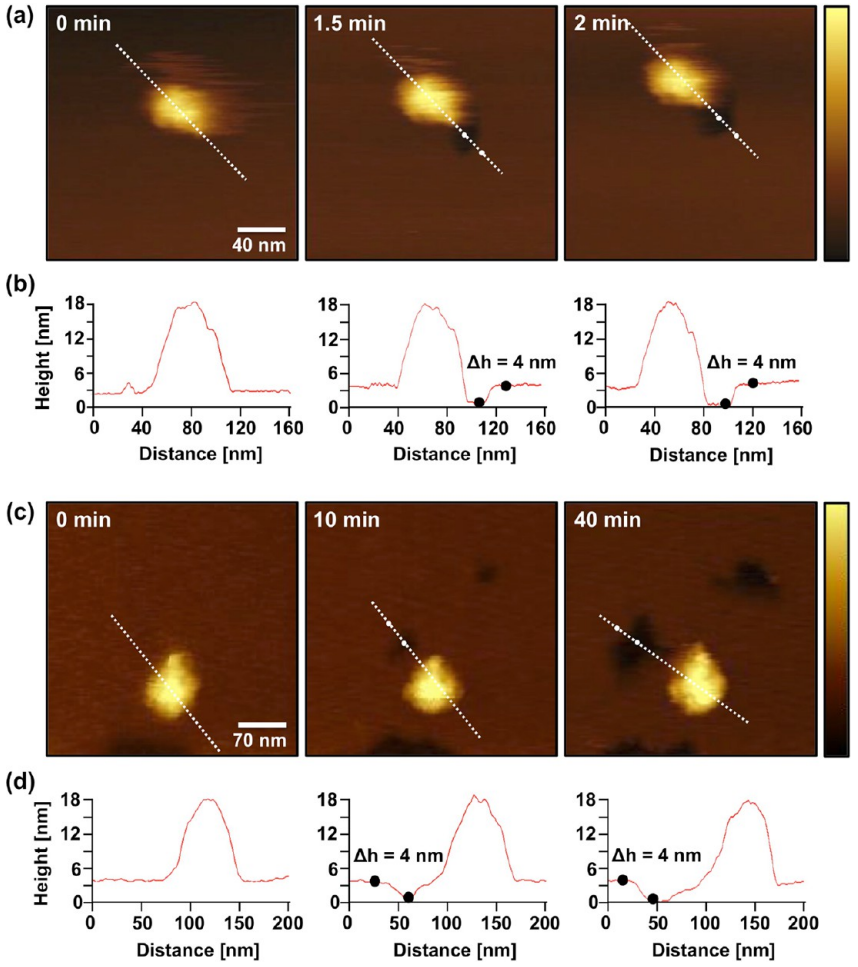

Figure 8. HS-AFM height images showing pore formation in the mito-MM caused by the Cytcox-KH_9/DNA complex (a) and the BP100-KH_9/DNA complex (c), with the height profiles along the dashed lines in (a), (b) and in (c), (d). The term "0 min" corresponds to 2.5 h in (a) and 2 h in (c) after the addition of 40 μL of complex into the imaging medium. Δh in (b) and (d) represents the height difference between the black circles, which correspond to the white circles on the dashed lines in (a) and (c). The color bar indicates the range of Z from 0 (darkest) to Z_{max} (brightest): Z_{max} = (a) 18 and (c) 20 nm.

necessary for tighter binding of peptides to the membrane.[56] Therefore, reduced hydrophobic interactions might be the reason, especially for BP100-KH_9 binding the mito-MM more weakly than the plasma-MM.

A comparison of the membrane binding affinities of the peptides and the peptide/DNA complexes showed that the difference in the binding affinities of the Cytcox-KH_9/DNA and BP100-KH_9/DNA complexes followed a tendency similar to that of Cytcox and BP100 rather than that of Cytcox-KH_9 and BP100-KH_9 (Table 1, Figure 2). This is evident from more of the BP100-KH_9/DNA complex than the Cytcox-KH_9/DNA complex binding to the mito-MM despite the similar K_a values obtained for Cytcox-KH_9 and BP100-KH_9 for the mito-MM. This suggests that the KH_9 domain did not take part in the membrane binding of the complex and confirms that the KH_9 domains were condensed in the complex interior, while Cytcox and BP100 were located in the periphery of the complex, facing the membrane surface. This result agrees well with a previous report on the DNA complex structures of Cytcox-KH_9.[22]

Effect of Membrane Fluidity and Surface Charge. While Cytcox and BP100 induced changes mostly in the DOPC-rich L_d phase of the plasma-MM (Figures 3 and 4), the Cytcox-KH_9/DNA and BP100-KH_9/DNA complexes localized on the DPPC-rich L_o domains of the membrane (Figure 6). The reason for the higher affinities of Cytcox and BP100 for the DOPC-rich phase of the membrane is likely the higher accessibility of the peptides to the phosphate groups and the acyl chains in the L_d phase. In the DPPC-rich phase, the accessible area was reduced by the high tilt angle of the phosphatidylcholine headgroups with respect to the membrane surface,[57,58] which results from the dense packing of lipids and a stable hydration layer on the DPPC-rich domains.[59] In addition, there are significant differences in the electrical potential of the two phases.[60−62] The DOPC membrane behaves like a negatively charged membrane because of an external field originating from the internal membrane dipole potential.[62] Since the membrane dipole potential significantly influences the peptide−membrane interaction,[63] we speculate that the higher membrane dipole potential of the DOPC-rich phase could be another factor facilitating the binding of these cationic peptides to this phase. In contrast to the cationic nature of the peptides used herein, their DNA complexes exhibit slightly negative zeta potentials. This may explain the localization of the Cytcox-KH_9/DNA and BP100-KH_9/DNA complexes on the L_o domains, where the positively charged choline groups of DPPC are oriented toward the solution and likely attract the complex.[57,58] The negative zeta potential of the complex is also possibly the reason for the lower amount of complex bound to the mito-MM than to the plasma-

https://dx.doi.org/10.1021/acs.langmuir.0c03320
Langmuir 2021, 37, 1882−1893

MM (Figure 2) despite the higher K_a values of both Cytcox and BP100 for the mito-MM than for the plasma-MM. The electrostatic repulsion between the anionic membrane and the complex might hamper the binding of the complex to the mito-MM.

Mechanism of Complex-Induced Membrane Disruption. Membrane fluidization and disruption caused by the Cytcox-KH_9/DNA and BP100-KH_9/DNA complexes (Figure 6) may indicate the release of Cytcox-KH_9 and BP100-KH_9 from the complexes upon membrane binding (Figure 7). On the basis of the HS-AFM images obtained for Cytcox-KH_9 and BP100-KH_9 (Figure 5), fluidization might have been caused by the parallel alignment of peptide molecules at the membrane interface below a critical surface concentration, and pore formation might have resulted from the increase in the local surface concentration of the released peptide. The question is whether peptide release is absolutely necessary for pore formation because the formation of membrane defects was also observed in the presence of amine-terminated silica nanoparticles,[64] which do not contain a flexible organic surface, and amphiphilic Janus nanoparticles[65] that were hydrophobic on one hemisphere and positively charged on the other by amine groups. This suggests that pore formation can be induced solely by deformation of the membrane and its subsequent rupture, resulting in lipid removal from the membrane. Based on this information, we may assume that the same mechanism takes place for the Cytcox-KH_9/DNA and BP100-KH_9/DNA complexes as well. However, because of the large size of the pores and the fluidization over a large area, the possibility of pore formation via membrane dissolution by the peptide released from the complex seems higher than the possibility of pore formation by membrane deformation.

In addition to the underlying mechanism for the complex-induced membrane disruption, we also need to pay attention to the differences in the pattern of disruption caused by the Cytcox-KH_9/DNA and BP100-KH_9/DNA complexes. The formation of expanding pores caused by the Cytcox-KH_9/DNA complex in the L_o domains (Figure S12) may indicate the release of a significant amount of peptide from the complex, leading to an abrupt increase in the membrane-bound peptide concentration in the vicinity of the complex. In contrast, the gradual disruption observed in the presence of the BP100-KH_9/DNA complex (Figure 6g–i) likely resulted from the slow release of the peptide and hence the higher stability of the BP100-KH_9/DNA complex than the Cytcox-KH_9/DNA complex on the plasma-MM. These differences can be attributed to Cytcox having a more disruptive nature than BP100 (Figures 3 and 4). Cytcox might be able to cause lipid removal in addition to membrane thinning, whereas BP100 caused only membrane thinning. The Cytcox-KH_9/DNA and BP100-KH_9/DNA complexes induced pore formation in the mito-MM as well (Figure 8), although the mito-MM was not ruptured by the peptides (Figures S6, S7). In this case, membrane deformation should be considered a possible mechanism of pore formation in the mito-MM by the complex. However, it is also possible that the complex, with a slightly negative zeta potential, induced the segregation of the anionic lipid-poor regions and the subsequent formation of pores in these regions by the released peptide, as was the case for the plasma-MM.

Comparison of the Complexes in Cellular and Mitochondrial Uptake. When the pore size and growth are considered, cellular uptake via direct membrane translocation is likely to be enhanced in the presence of the Cytcox-KH_9/DNA complex due to the formation of expanding pores by this complex. However, pore formation does not correlate with the gene delivery efficiency; instead, it may elevate cytotoxicity.[66,67] In the determination of the efficiency of the carrier peptide in gene delivery, its membrane binding affinity might be more critical than its disruption ability. Thus, the higher binding affinity for BP100 than for Cytcox is possibly one of the reasons for the increased gene delivery efficiency in plant cells in the presence of BP100 and might be able to improve gene delivery in mammalian cells as well. Because of the localization of the Cytcox-KH_9/DNA and BP100-KH_9/DNA complexes on the L_o domains, resembling the raftlike domains in the plasma membrane, we suggest that raft-mediated endocytosis[68,69] can be an uptake pathway for complexes smaller than lipid rafts. In the case of the mito-MM, we observed DNA-like features in the disrupted regions of the membrane after prolonged incubation (Figure S13a), suggesting that Cytcox-KH_9 might transport and release plasmid DNA into the mitochondrial matrix. Although BP100-KH_9 was not as efficient as Cytcox-KH_9 in releasing the plasmid DNA (Figures S13b, c), the higher amount of membrane-bound BP100-KH_9/DNA complex than Cytcox-KH_9/DNA complex (Figure 2b) implies that the inclusion of BP100 in the Cytcox-KH_9/DNA complex may increase the complex abundance on the mitochondrial membrane, similar to the plasma membrane. Nonetheless, the action of the Cytcox-KH_9/DNA complex would be more critical in the cytosol than the action of the complex with BP100 because of the crucial role of Cytcox in targeting the mitochondria.

CONCLUSIONS

In summary, we compared the membrane activities of two carrier peptides (Cytcox and BP100) and their DNA complexes on model lipid membranes mimicking the mammalian plasma membrane or the mitochondrial outer membrane using two surface characterization techniques, QCM and HS-AFM. We have revealed that Cytcox, which is a mitochondria-targeting peptide, exhibits a lower membrane binding affinity than BP100, which is a CPP. Interestingly, the DNA-carrying complex of Cytcox seemed to be more membrane disruptive than that of BP100. The former's high membrane-disrupting activity can be advantageous for the rapid cellular uptake of the complex via direct translocation across the plasma membrane and for the release of plasmid DNA into the mitochondria. However, the higher binding affinity of BP100 increases the probability of internalizing a higher number of complexes into the cell via endocytosis and/or direct translocation. Our results together with the findings in a previous study[23] that reported an improvement in the gene transfection efficiency of the Cytcox-KH_9/DNA complex when modified with BP100 suggest that the binding affinity of the peptide/DNA complex for the plasma membrane is likely more critical in enhancing the gene transfection efficiency than the membrane-disrupting activity of the complex. The latter might actually elevate cytotoxicity if the membrane cannot reseal after complex entry into the cell. All these findings revealing the differences in the membrane activities of the carrier peptides and their DNA complexes confirm the important role of CPPs in gene delivery and may help to improve the design of an efficient peptide-based organelle-specific gene delivery system.

https://dx.doi.org/10.1021/acs.langmuir.0c03320
Langmuir 2021, 37, 1882−1893

■ ASSOCIATED CONTENT

Supporting Information

) The Supporting Information is available free of charge at https://pubs.acs.org/doi/10.1021/acs.langmuir.0c03320.

Time-course plots of peptide binding to the plasma-MM and the mito-MM; morphological changes in the plasma-MM and mito-MM in the presence of the different peptides; membrane defects; pore formation in the plasma-MM in the presence of Cytcox-KH_9 and BP100-KH_9; size and zeta potential of Cytcox-KH_9/DNA and BP100-KH_9/DNA complexes; Cytcox-KH_9/DNA and BP100-KH_9/DNA complexes inserted into the plasma-MM; loosening in the Cytcox-KH_9/DNA complex at reduced pH; complex localization on the membrane and complex-induced membrane fluidization; expanding pores in the plasma-MM in the presence of the Cytcox-KH_9/DNA complex; disruption of the mito-MM by Cytcox-KH_9/DNA and BP100-KH_9/DNA complexes (PDF)

Changes in the plasma-MM in the presence of Cytcox (MOV)

Changes in the plasma-MM in the presence of BP100 (MOV)

Changes in the plasma-MM in the presence of Cytcox-KH_9 (MOV)

Changes in the plasma-MM in the presence of BP100-KH_9 (MOV)

Changes in the plasma-MM in the presence of BP100-KH_9 (MOV)

Changes in the mito-MM in the presence of Cytcox-KH_9 (MOV)

Changes in the mito-MM in the presence of BP100-KH_9 (MOV)

■ AUTHOR INFORMATION

Corresponding Author

Keiji Numata − *Biomacromolecules Research Team, RIKEN Center for Sustainable Resource Science, Wako, Saitama 351-0198, Japan; Laboratory for Biomaterial Chemistry, Department of Material Chemistry, Graduate School of Engineering, Kyoto University, Kyoto 606-8501, Japan;* orcid.org/0000-0003-2199-7420; Email: numata.keiji.3n@kyoto-u.ac.jp

Authors

Neval Yilmaz − *Biomacromolecules Research Team, RIKEN Center for Sustainable Resource Science, Wako, Saitama 351-0198, Japan*

Yutaka Kodama − *Biomacromolecules Research Team, RIKEN Center for Sustainable Resource Science, Wako, Saitama 351-0198, Japan; Center for Bioscience Research & Education, Utsunomiya University, Tochigi 321-8505, Japan*

Complete contact information is available at: https://pubs.acs.org/10.1021/acs.langmuir.0c03320

Notes

The authors declare no competing financial interest.

■ ACKNOWLEDGMENTS

This work was supported by JST ERATO grant number JPMJER1602, Japan.

■ REFERENCES

(1) Cartier, R.; Reszka, R. Utilization of Synthetic Peptides Containing Nuclear Localization Signals for Nonviral Gene Transfer Systems. *Gene Ther.* **2002**, *9* (3), 157−167.

(2) Numata, K. Poly(Amino Acid)s/Polypeptides as Potential Functional and Structural Materials. *Polym. J.* **2015**, *47* (8), 537−545.

(3) Yin, H.; Kanasty, R. L.; Eltoukhy, A. A.; Vegas, A. J.; Dorkin, J. R.; Anderson, D. G. Non-Viral Vectors for Gene-Based Therapy. *Nat. Rev. Genet.* **2014**, *15* (8), 541−555.

(4) Böhmová, E.; Machová, D.; Pechar, M.; Pola, R.; Venclíková, K.; Janoušková, O.; Etrych, T. Cell-Penetrating Peptides: A Useful Tool for the Delivery of Various Cargoes Into Cells. *Physiol. Res.* **2018**, S267−S279.

(5) Chugh, A.; Eudes, F.; Shim, Y.-S. Cell-Penetrating Peptides: Nanocarrier for Macromolecule Delivery in Living Cells. *IUBMB Life* **2010**, *62* (3), 183−193.

(6) Habault, J.; Poyet, J.-L. Recent Advances in Cell Penetrating Peptide-Based Anticancer Therapies. *Molecules* **2019**, *24* (5), 927.

(7) Numata, K.; Horii, Y.; Oikawa, K.; Miyagi, Y.; Demura, T.; Ohtani, M. Library Screening of Cell-Penetrating Peptide for BY-2 Cells, Leaves of Arabidopsis, Tobacco, Tomato, Poplar, and Rice Callus. *Sci. Rep.* **2018**, *8* (10966), 1−17.

(8) Terada, K.; Gimenez-Dejoz, J.; Miyagi, Y.; Oikawa, K.; Tsuchiya, K.; Numata, K. Artificial Cell-Penetrating Peptide Containing Periodic Alpha-Aminoisobutyric Acid with Long-Term Internalization Efficiency in Human and Plant Cells. *ACS Biomater. Sci. Eng.* **2020**, *6* (6), 3287−3298.

(9) Kauffman, W. B.; Fuselier, T.; He, J.; Wimley, W. C. Mechanism Matters: A Taxonomy of Cell Penetrating Peptides. *Trends Biochem. Sci.* **2015**, *40* (12), 749−764.

(10) Kim, S.; Nam, H. Y.; Lee, J.; Seo, J. Mitochondrion-Targeting Peptides and Peptidomimetics: Recent Progress and Design Principles. *Biochemistry* **2020**, *59* (3), 270−284.

(11) Yoshizumi, T.; Oikawa, K.; Chuah, J. A.; Kodama, Y.; Numata, K. Selective Gene Delivery for Integrating Exogenous DNA into Plastid and Mitochondria! Genomes Using Peptide-DNA Complexes. *Biomacromolecules* **2018**, *19* (5), 1582−1591.

(12) Thagun, C.; Chuah, J. A.; Numata, K. Targeted Gene Delivery into Various Plastids Mediated by Clustered Cell-Penetrating and Chloroplast-Targeting Peptides. *Adv. Sci.* **2019**, *6*, 1902064.

(13) Morris, V. J.; Kirby, A. R.; Gunning, A. P. *Atomic Force Microscopy for Biologists*, 2nd ed.; Imperial College Press: London, 2010; pp 76−341.

(14) Hammond, K.; Ryadnov, M. G.; Hoogenboom, B. W. Atomic Force Microscopy to Elucidate How Peptides Disrupt Membranes. *Biochim. Biophys. Acta, Biomembr.* **2021**, *1863*, 183447.

(15) Deshayes, S.; Plénat, T.; Aldrian-Herrada, G.; Divita, G.; Le Grimellec, C.; Heitz, F. Primary Amphipathic Cell-Penetrating Peptides: Structural Requirements and Interactions with Model Membranes †. *Biochemistry* **2004**, *43* (24), 7698−7706.

(16) Herbig, M. E.; Assi, F.; Textor, M.; Merkle, H. P. The Cell Penetrating Peptides PVEC and W2-PVEC Induce Transformation of Gel Phase Domains in Phospholipid Bilayers without Affecting Their Integrity. *Biochemistry* **2006**, *45* (11), 3598−3609.

(17) Plénat, T.; Boichot, S.; Dosset, P.; Milhiet, P.-E.; Le Grimellec, C. Coexistence of a Two-States Organization for a Cell-Penetrating Peptide in Lipid Bilayer. *Biophys. J.* **2005**, *89* (6), 4300−4309.

(18) Plénat, T.; Deshayes, S.; Boichot, S.; Milhiet, P. E.; Cole, R. B.; Heitz, F.; Le Grimellec, C. Interaction of Primary Amphipathic Cell-Penetrating Peptides with Phospholipid-Supported Monolayers. *Langmuir* **2004**, *20* (21), 9255−9261.

(19) Russell, O.; Turnbull, D. Mitochondrial DNA Disease—Molecular Insights and Potential Routes to a Cure. *Exp. Cell Res.* **2014**, *325* (1), 38−43.

(20) Hurt, E. C.; Pesold-Hurt, B.; Suda, K.; Oppliger, W.; Schatz, G. The First Twelve Amino Acids (Less than Half of the Pre-Sequence) of an Imported Mitochondrial Protein Can Direct Mouse Cytosolic Dihydrofolate Reductase into the Yeast Mitochondrial Matrix. *EMBO J.* **1985**, *4* (8), 2061−2068.

(21) Chen, Q.-R.; Zhang, L.; Stass, S. A.; Mixson, A. J. Co-Polymer of Histidine and Lysine Markedly Enhances Transfection Efficiency of Liposomes. *Gene Ther.* **2000**, *7* (19), 1698−1705.
(22) Chuah, J.-A.; Matsugami, A.; Hayashi, F.; Numata, K. Self-Assembled Peptide-Based System for Mitochondrial-Targeted Gene Delivery: Functional and Structural Insights. *Biomacromolecules* **2016**, *17* (11), 3547−3557.
(23) Chuah, J.-A.; Yoshizumi, T.; Kodama, Y.; Numata, K. Gene Introduction into the Mitochondria of Arabidopsis Thaliana via Peptide-Based Carriers. *Sci. Rep.* **2015**, *5* (7751), 1−7.
(24) Eggenberger, K.; Mink, C.; Wadhwani, P.; Ulrich, A. S.; Nick, P. Using the Peptide Bp100 as a Cell-Penetrating Tool for the Chemical Engineering of Actin Filaments within Living Plant Cells. *ChemBioChem* **2011**, *12* (1), 132−137.
(25) Lakshmanan, M.; Kodama, Y.; Yoshizumi, T.; Sudesh, K.; Numata, K. Rapid and Efficient Gene Delivery into Plant Cells Using Designed Peptide Carriers. *Biomacromolecules* **2013**, *14* (1), 10−16.
(26) Midorikawa, K.; Kodama, Y.; Numata, K. Vacuum/Compression Infiltration-Mediated Permeation Pathway of a Peptide-PDNA Complex as a Non-Viral Carrier for Gene Delivery in Planta. *Sci. Rep.* **2019**, *9* (271), 1−10.
(27) Xu, X.; London, E. The Effect of Sterol Structure on Membrane Lipid Domains Reveals How Cholesterol Can Induce Lipid Domain Formation. *Biochemistry* **2000**, *39* (5), 843−849.
(28) Rinia, H. A.; Snel, M. M. E.; van der Eerden, J. P. J. M.; de Kruijff, B. Visualizing Detergent Resistant Domains in Model Membranes with Atomic Force Microscopy. *FEBS Lett.* **2001**, *501* (1), 92−96.
(29) Veatch, S. L.; Keller, S. L. Separation of Liquid Phases in Giant Vesicles of Ternary Mixtures of Phospholipids and Cholesterol. *Biophys. J.* **2003**, *85* (5), 3074−3083.
(30) Kuwana, T.; Mackey, M. R.; Perkins, G.; Ellisman, M. H.; Latterich, M.; Schneiter, R.; Green, D. R.; Newmeyer, D. D. Bid, Bax, and Lipids Cooperate to Form Supramolecular Openings in the Outer Mitochondrial Membrane. *Cell* **2002**, *111* (3), 331−342.
(31) Horvath, S. E.; Daum, G. Lipids of Mitochondria. *Prog. Lipid Res.* **2013**, *52* (4), 590−614.
(32) Salvador-Gallego, R.; Mund, M.; Cosentino, K.; Schneider, J.; Unsay, J.; Schraermeyer, U.; Engelhardt, J.; Ries, J.; García-Sáez, A. J. Bax Assembly into Rings and Arcs in Apoptotic Mitochondria Is Linked to Membrane Pores. *EMBO J.* **2016**, *35* (4), 389−401.
(33) Ando, T.; Uchihashi, T.; Scheuring, S. Filming Biomolecular Processes by High-Speed Atomic Force Microscopy. *Chem. Rev.* **2014**, *114* (6), 3120−3188.
(34) Kamihira, M.; Nakazawa, H.; Kira, A.; Mizutani, Y.; Nakamura, M.; Nakayama, T. Interaction of Tea Catechins with Lipid Bilayers Investigated by a Quartz-Crystal Microbalance Analysis. *Biosci., Biotechnol., Biochem.* **2008**, *72* (5), 1372−1375.
(35) Miyamoto, T.; Tsuchiya, K.; Numata, K. Block Copolymer/Plasmid DNA Micelles Postmodified with Functional Peptides via Thiol−Maleimide Conjugation for Efficient Gene Delivery into Plants. *Biomacromolecules* **2019**, *20* (2), 653−661.
(36) Nečas, D.; Klapetek, P. Gwyddion: An Open-Source Software for SPM Data Analysis. *Cent. Eur. J. Phys.* **2012**, *10* (1), 181−188.
(37) Colotto, A.; Martin, I.; Ruysschaert, J.-M.; Sen, A.; Epand, R. M. Structural Study of the Interaction Between the Mitochondrial Presequence of Cytochrome c Oxidase Subunit IV and Model Membranes. *Biosci. Rep.* **1998**, *18* (5), 251−263.
(38) Roise, D.; Horvath, S. J.; Tomich, J. M.; Richards, J. H.; Schatz, G. A Chemically Synthesized Pre-Sequence of an Imported Mitochondrial Protein Can Form an Amphiphilic Helix and Perturb Natural and Artificial Phospholipid Bilayers. *EMBO J.* **1986**, *5* (6), 1327−1334.
(39) Tamm, L. K. Incorporation of a Synthetic Mitochondrial Signal Peptide into Charged and Uncharged Phospholipid Monolayers. *Biochemistry* **1986**, *25* (23), 7470−7476.
(40) Manzini, M. C.; Perez, K. R.; Riske, K. A.; Bozelli, J. C.; Santos, T. L.; da Silva, M. A.; Saraiva, G. K. V.; Politi, M. J.; Valente, A. P.; Almeida, F. C. L.; Chaimovich, H.; Rodrigues, M. A.; Bemquerer, M. P.; Schreier, S.; Cuccovia, I. M. Peptide:Lipid Ratio and Membrane Surface Charge Determine the Mechanism of Action of the Antimicrobial Peptide BP100. Conformational and Functional Studies. *Biochim. Biophys. Acta, Biomembr.* **2014**, *1838* (7), 1985−1999.
(41) Park, P.; Franco, L. R.; Chaimovich, H.; Coutinho, K.; Cuccovia, I. M.; Lima, F. S. Binding and Flip as Initial Steps for BP-100 Antimicrobial Actions. *Sci. Rep.* **2019**, *9* (8622), 1−14.
(42) Davis, J. H.; Clair, J. J.; Juhasz, J. Phase Equilibria in DOPC/DPPC-D62/Cholesterol Mixtures. *Biophys. J.* **2009**, *96* (2), 521−539.
(43) Sankaram, M. B.; Thompson, T. E. Cholesterol-Induced Fluid-Phase Immiscibility in Membranes. *Proc. Natl. Acad. Sci. U. S. A.* **1991**, *88* (19), 8686−8690.
(44) Henderson, J. M.; Waring, A. J.; Separovic, F.; Lee, K. Y. C. Antimicrobial Peptides Share a Common Interaction Driven by Membrane Line Tension Reduction. *Biophys. J.* **2016**, *111* (10), 2176−2189.
(45) Lam, K. L. H.; Wang, H.; Siaw, T. A.; Chapman, M. R.; Waring, A. J.; Kindt, J. T.; Lee, K. Y. C. Mechanism of Structural Transformations Induced by Antimicrobial Peptides in Lipid Membranes. *Biochim. Biophys. Acta, Biomembr.* **2012**, *1818* (2), 194−204.
(46) Mecke, A.; Lee, D.-K.; Ramamoorthy, A.; Orr, B. G.; Banaszak Holl, M. M. Membrane Thinning Due to Antimicrobial Peptide Binding: An Atomic Force Microscopy Study of MSI-78 in Lipid Bilayers. *Biophys. J.* **2005**, *89* (6), 4043−4050.
(47) Shaw, J. E.; Alattia, J.-R.; Verity, J. E.; Privé, G. G.; Yip, C. M. Mechanisms of Antimicrobial Peptide Action: Studies of Indolicidin Assembly at Model Membrane Interfaces by in Situ Atomic Force Microscopy. *J. Struct. Biol.* **2006**, *154* (1), 42−58.
(48) Misiewicz, J.; Afonin, S.; Grage, S. L.; van den Berg, J.; Strandberg, E.; Wadhwani, P.; Ulrich, A. S. Action of the Multifunctional Peptide BP100 on Native Biomembranes Examined by Solid-State NMR. *J. Biomol. NMR* **2015**, *61* (3−4), 287−298.
(49) Heath, G. R.; Harrison, P. L.; Strong, P. N.; Evans, S. D.; Miller, K. Visualization of Diffusion Limited Antimicrobial Peptide Attack on Supported Lipid Membranes. *Soft Matter* **2018**, *14* (29), 6146−6154.
(50) Huang, K.; García, A. E. Free Energy of Translocating an Arginine-Rich Cell-Penetrating Peptide across a Lipid Bilayer Suggests Pore Formation. *Biophys. J.* **2013**, *104* (2), 412−420.
(51) Allolio, C.; Magarkar, A.; Jurkiewicz, P.; Baxová, K.; Javanainen, M.; Mason, P. E.; Šachl, R.; Cebecauer, M.; Hof, M.; Horinek, D.; Heinz, V.; Rachel, R.; Ziegler, C. M.; Schröfel, A.; Jungwirth, P. Arginine-Rich Cell-Penetrating Peptides Induce Membrane Multilamellarity and Subsequently Enter via Formation of a Fusion Pore. *Proc. Natl. Acad. Sci. U. S. A.* **2018**, *115* (47), 11923−11928.
(52) Epand, R. F.; Maloy, W. L.; Ramamoorthy, A.; Epand, R. M. Probing the "Charge Cluster Mechanism" in Amphipathic Helical Cationic Antimicrobial Peptides. *Biochemistry* **2010**, *49* (19), 4076−4084.
(53) Herce, H. D.; Garcia, A. E.; Litt, J.; Kane, R. S.; Martin, P.; Enrique, N.; Rebolledo, A.; Milesi, V. Arginine-Rich Peptides Destabilize the Plasma Membrane, Consistent with a Pore Formation Translocation Mechanism of Cell-Penetrating Peptides. *Biophys. J.* **2009**, *97* (7), 1917−1925.
(54) Ulmschneider, J. P. Charged Antimicrobial Peptides Can Translocate across Membranes without Forming Channel-like Pores. *Biophys. J.* **2017**, *113* (1), 73−81.
(55) Grage, S. L.; Afonin, S.; Ulrich, A. S. Dynamic Transitions of Membrane-Active Peptides. In *Antimicrobial Peptides*; Giuliani, A., Rinaldi, A. C., Eds.; Methods in Molecular Biology; Humana Press: Totowa, NJ, 2010; Vol. *618*, pp 183−207. DOI: 10.1007/978-1-60761-594-1_13.
(56) Ladokhin, A. S.; White, S. H. Protein Chemistry at Membrane Interfaces: Non-Additivity of Electrostatic and Hydrophobic Interactions. *J. Mol. Biol.* **2001**, *309* (3), 543−552.
(57) Asakawa, H.; Yoshioka, S.; Nishimura, K.; Fukuma, T. Spatial Distribution of Lipid Headgroups and Water Molecules at Membrane/Water Interfaces Visualized by Three-Dimensional Scanning Force Microscopy. *ACS Nano* **2012**, *6* (10), 9013−9020.

https://dx.doi.org/10.1021/acs.langmuir.0c03320
Langmuir 2021, 37, 1882−1893

(58) Pink, D. A.; Belaya, M.; Levadny, V.; Quinn, B. A Model of Polar Group Statics in Lipid Bilayers and Monolayers. *Langmuir* **1997**, *13* (6), 1701−1711.
(59) Sheikh, K. H.; Jarvis, S. P. Crystalline Hydration Structure at the Membrane−Fluid Interface of Model Lipid Rafts Indicates a Highly Reactive Boundary Region. *J. Am. Chem. Soc.* **2011**, *133* (45), 18296−18303.
(60) Makino, K.; Yamada, T.; Kimura, M.; Oka, T.; Ohshima, H.; Kondo, T. Temperature- and Ionic Strength-Induced Conformational Changes in the Lipid Head Group Region of Liposomes as Suggested by Zeta Potential Data. *Biophys. Chem.* **1991**, *41* (2), 175−183.
(61) Wang, L. Measurements and Implications of the Membrane Dipole Potential. *Annu. Rev. Biochem.* **2012**, *81* (1), 615−635.
(62) Yang, Y.; Mayer, K. M.; Wickremasinghe, N. S.; Hafner, J. H. Probing the Lipid Membrane Dipole Potential by Atomic Force Microscopy. *Biophys. J.* **2008**, *95* (11), 5193−5199.
(63) Zhan, H.; Lazaridis, T. Influence of the Membrane Dipole Potential on Peptide Binding to Lipid Bilayers. *Biophys. Chem.* **2012**, *161*, 1−7.
(64) Leroueil, P. R.; Berry, S. A.; Duthie, K.; Han, G.; Rotello, V. M.; McNerny, D. Q.; Baker, J. R.; Orr, B. G.; Banaszak Holl, M. M. Wide Varieties of Cationic Nanoparticles Induce Defects in Supported Lipid Bilayers. *Nano Lett.* **2008**, *8* (2), 420−424.
(65) Lee, K.; Zhang, L.; Yi, Y.; Wang, X.; Yu, Y. Rupture of Lipid Membranes Induced by Amphiphilic Janus Nanoparticles. *ACS Nano* **2018**, *12* (4), 3646−3657.
(66) Vaidyanathan, S.; Anderson, K. B.; Merzel, R. L.; Jacobovitz, B.; Kaushik, M. P.; Kelly, C. N.; van Dongen, M. A.; Dougherty, C. A.; Orr, B. G.; Banaszak Holl, M. M. Quantitative Measurement of Cationic Polymer Vector and Polymer−PDNA Polyplex Intercalation into the Cell Plasma Membrane. *ACS Nano* **2015**, *9* (6), 6097−6109.
(67) Vaidyanathan, S.; Orr, B. G.; Banaszak Holl, M. M. Role of Cell Membrane−Vector Interactions in Successful Gene Delivery. *Acc. Chem. Res.* **2016**, *49* (8), 1486−1493.
(68) El-Sayed, A.; Harashima, H. Endocytosis of Gene Delivery Vectors: From Clathrin-Dependent to Lipid Raft-Mediated Endocytosis. *Mol. Ther.* **2013**, *21* (6), 1118−1130.
(69) Wadia, J. S.; Stan, R. V.; Dowdy, S. F. Transducible TAT-HA Fusogenic Peptide Enhances Escape of TAT-Fusion Proteins after Lipid Raft Macropinocytosis. *Nat. Med.* **2004**, *10* (3), 310−315.

https://dx.doi.org/10.1021/acs.langmuir.0c03320
Langmuir 2021, 37, 1882−1893